CrossMark

# Isotope Dichotomy from Solar Protoplanetary Disk Processing of $^{150}$Nd-rich Stellar Ejecta

Nikitha Susan Saji [ORCID], Martin Schiller [ORCID], Jesper Christian Holst, and Martin Bizzarro [ORCID]
Centre for Star and Planet Formation, Globe Institute, University of Copenhagen, DK-1350 Copenhagen, Denmark; nikitha.saji@sund.ku.dk
Received 2021 April 8; revised 2021 August 4; accepted 2021 August 17; published 2021 September 21

## Abstract

We use high-precision neodymium isotope data for sequentially acid-leached components of the primitive carbonaceous chondrite Tagish Lake to identify a non-classical $^{150}$Nd-rich presolar carrier phase that has not been identified as of yet in meteorites. The distinct isotopic signature of this carrier can be attributed to the intermediate neutron capture process ($i$-process) occurring in asymptotic giant branch (AGB), super-AGB, or post-AGB stars or, alternatively, the slow capture process ($s$-process) occurring in rotating massive stars. The $^{150}$Nd-rich carrier appears to be heterogeneously distributed in the solar protoplanetary disk resulting in systematic isotope variations between carbonaceous and non-carbonaceous solar system materials. Carbonaceous chondrites that accreted in the outer disk are depleted in this carrier relative to non-carbonaceous materials that accreted in the terrestrial planet-forming region. Calcium-aluminum-rich inclusions that represent the earliest formed disk solids record the largest depletion of this carrier. This distribution pattern is contrary to that seen for the carriers of other neutron-rich isotope anomalies ($^{48}$Ca, $^{54}$Cr, $^{95,97}$Mo, etc.) that have defined carbonaceous/non-carbonaceous isotope dichotomy so far. Irrespective of the exact astrophysical origin of these carriers, divergent distribution of presolar dust as a function of physicochemical processing in the solar protoplanetary disk best explains the solar system isotope dichotomy as opposed to changes in the composition of the infall.

Unified Astronomy Thesaurus concepts: Meteorites (1038); Circumstellar dust (236)

## 1. Introduction

A growing number of studies have documented isotopic variability within solar system materials presumably from heterogeneous distribution of presolar dust in the solar proto-planetary disk (e.g., Dauphas et al. 2002; Trinquier et al. 2007). Some of these variations have been attributed to selective destruction of presolar dust grains in the inner disk regions during the early phases of disk evolution (Trinquier et al. 2009; Van Kooten et al. 2016; Schiller et al. 2018). Alternatively, isotope variations could reflect primordial spatial and/or temporal heterogeneities in presolar dust distribution preserved due to planet-carved gaps (Nanne et al. 2019) or distinct bursts of planetesimal formation related to migration of the snow line (Lichtenberg et al. 2021).

Much uncertainty exists regarding the inventory of presolar dust populations that were initially present in the protosolar molecular cloud and their eventual aggregation into planets and planetesimals. Nucleosynthetic anomalies in trans-Fe elements such as Zr, Mo, Ru, Pd, Ba, Nd, and Sm have been primarily linked to heterogeneous distribution of dust from asymptotic giant branch (AGB) stars, which are the main sites of slow neutron capture ($s$-process) nucleosynthesis (Burkhardt et al. 2011; Akram et al. 2015; Fischer-Gödde et al. 2015; Burkhardt et al. 2016; Fukai & Yokoyama 2017; Ek et al. 2019; Saji et al. 2020). On the other hand, variations in neutron-rich isotopes produced in high neutron density stellar environments such as $^{48}$Ca, $^{50}$Ti, $^{54}$Cr, $^{58}$Ni, etc., as well as those isotopes of Mo considered to be produced by rapid neutron capture ($r$-process) nucleosynthesis, have been linked to ejecta from supernova

explosions (Trinquier et al. 2007; Warren 2011; Steele et al. 2012; Schiller et al. 2015; Budde et al. 2016; Nanne et al. 2019). Although presolar grains bearing pure $s$-process signatures have been recovered from meteorites for decades (e.g., Richter et al. 1992; Hoppe et al. 1997; Ott 1999), very little is currently known regarding the carriers of neutron-rich and $r$-process isotope anomalies (Nittler et al. 2018).

Constraining the inventory of presolar dust populations in the protosolar molecular cloud is important toward understanding the astronomical context of solar system formation as well as the origin of its planetary-scale isotope variations. Here, we use Nd isotopes in the sequentially acid-leached components of primitive carbonaceous chondrite Tagish Lake to identify presolar carriers that constitute the solar system inventory of heavy elements. We find unambiguous evidence for a non-classical nucleosynthetic component that has not been identified as of yet in meteorites, in addition to the ubiquitous classical $s$-process Nd component. This component, whose $^{150}$Nd-enriched composition can be described by intermediate neutron capture nucleosynthesis (Cowan & Rose 1977; Hampel et al. 2016; Roederer et al. 2016) or slow neutron capture nucleosynthesis in rotating massive stars (Frischknecht et al. 2015; Prantzos et al. 2019), appears to be heterogeneously distributed in the solar protoplanetary disk resulting in the apparent bifurcation of solar system materials into carbonaceous and non-carbonaceous suites.

## 2. Methods

We subjected a powdered sample of carbonaceous chondrite Tagish Lake weighing 1.75 g to a step-wise acid-leaching procedure that involves 12 increments of digestion in progressively stronger reagents to chemically separate potential isotopically anomalous presolar carriers (Table 1). This represents the first high-resolution step leaching study of a

**Table 1**
The Sequential Leaching Protocol Used for Tagish Lake Meteorite

| Leach Step | Reagent | Duration | T (°C) |
|---|---|---|---|
| L1 | MQ $H_2O$ | 30 minutes | 20 |
| L2 | 0.4 M HAc | 30 minutes | 20 |
| L3 | 8.5 M HAc | 1 day | 20 |
| L4 | 0.5 M $HNO_3$ | 10 minutes | 20 |
| L5 | 1 M $HNO_3$ | 1 hr | 20 |
| L6 | 4 M $HNO_3$ | 1 day | 20 |
| L7 | 7 M $HNO_3$ | 1 day | 20 |
| L8 | 6 M HCl | 1 day | 35 |
| L9 | 6 M HCl | 1 day | 80 |
| L10 | 3 M HCl + 13 M HF | 4 days | 100 |
| L11 | 7 M $HNO_3$ + 13 M HF | 10 days | 150 |
| L12 | 7 M $HNO_3$ + 13 M HF | 3 days (Parr bomb) | 210 |

primitive carbonaceous chondrite aimed at identifying presolar Nd isotope carriers. The early leaching steps in which we use weak acids (L1–L6) yield fractions that dissolve easily soluble phases such as carbonates and sulfides, whereas silicates, metal, and possibly oxides undergo dissolution in the later leaching steps that use strong acids (L7–L11). The most acid-resistant refractory phases contained in the residue (L12) are dissolved by high pressure digestion in Parr bomb vessels. This leaching protocol is more elaborate than that used in previous Nd isotope meteorite leaching experiments (e.g., Qin et al. 2011; Boyet & Gannoun 2013). Neodymium was purified from each leach fraction following the protocol described in Saji et al. (2016) and Saji et al. (2020). The leach fractions L1, L11, and L12 contained too little Nd to be analyzed separately and hence were combined with the preceding or following fractions, namely L2 and L10. Total Nd procedural blanks were less than 0.01 ng and the analyzed fractions contained between ∼0.7 and 770 ng Nd (Table 2).

Neodymium isotopes were measured using a ThermoFisher Neptune Plus multicollector inductively coupled plasma mass spectrometer located at Centre for Star and Planet Formation (Copenhagen). Samples were dissolved in 2% $HNO_3$ and introduced into the plasma source via ESI Apex IR sample introduction system at uptake rates of 0.02–0.04 mL minute$^{-1}$. The seven Nd isotopes $^{142}$Nd, $^{143}$Nd, $^{144}$Nd, $^{145}$Nd, $^{146}$Nd, $^{148}$Nd, and $^{150}$Nd were measured in static low-resolution mode with Faraday cups connected to $10^{11}\Omega$ amplifiers. Isobaric interferences from Ce and Sm were corrected for by monitoring $^{140}$Ce and $^{147}$Sm using $10^{12}\Omega$ amplifiers. Given their low Nd content, most fractions could be analyzed only once, except L3, which contained enough Nd to be analyzed 10 times. Each analysis consisted of 35–50 cycles of measurement with an integration interval of 8.34 s for each cycle, and each sample analysis was bracketed by JNdi-1 analyses. Instrumental mass fractionation was corrected by internal normalization to $^{146}$Nd/$^{144}$Nd, $^{148}$Nd/$^{144}$Nd, as well as $^{148}$Nd/$^{145}$Nd ratios so that nucleosynthetic variability on different Nd isotopes could be identified (Tables 2 and 3). Nd isotope data are reported as parts per million deviations of the $^i$Nd/$^{144}$Nd ratio from that of the JNdi-1 Nd isotope standard in $\mu$ notation. The $^{147}$Sm/$^{144}$Nd ratios of leach fractions were determined directly on bulk aliquots without isotope dilution by external sample-standard-bracketing using a mixed Alfa Cesar Sm-Nd standard. The accuracy of this protocol was evaluated by repeat analyses of BCR-2 and BHVO-2 terrestrial standards, and the obtained $^{147}$Sm/$^{144}$Nd ratios are accurate to 5%.

## 3. Neodymium Isotopes in Tagish Lake Leaches and Residue

Previous Nd isotope measurements on the leaches and residue obtained by step-wise dissolution of primitive meteorites reveal the influence of mainstream SiC grains that carry pure *s*-process signatures (Qin et al. 2011; Boyet & Gannoun 2013). The first three leaching steps of Boyet & Gannoun (2013) are similar to that we adopt in this study, and constitute ∼55% to 95% of total Nd depending on the meteorite mineralogy. These early fractions are characterized by deficits in $\mu^{142}$Nd, and excesses in $\mu^{145}$Nd, $\mu^{148}$Nd, and $\mu^{150}$Nd during normalization to $^{146}$Nd/$^{144}$Nd (Table 2 and Figure 1(b)). This anomaly pattern is broadly consistent with that obtained by subtraction of *s*-process Nd component from (or addition of *r*-process Nd component to) average solar Nd (Arlandini et al. 1999). Nevertheless, an intriguing feature becomes apparent upon normalization to $^{148}$Nd/$^{144}$Nd. The $\mu^{150}$Nd compositions of early fractions (L1 to L6) are either terrestrial or largely negative when normalized to $^{148}$Nd/$^{144}$Nd ratio (Table 3 and Figure 1(a)). As such, negative $\mu^{150}$Nd values coexisting with positive $\mu^{145}$Nd and negative $\mu^{142,146}$Nd compositions is inconsistent with pure *s*-process deficit. This is because $^{150}$Nd is considered to be produced exclusively by the *r*-process that operates at high neutron density environments (Bisterzo et al. 2011, 2015). A deficit in *s*-process Nd relative to solar composition as signified by positive $\mu^{145}$Nd and negative $\mu^{142,146}$Nd values in the early fractions should show a commensurate excess in $\mu^{150}$Nd, contrary to what is seen here (Figure 1(a)). Note that *s*-deficit and *r*-excess patterns cannot be distinguished from each other for Nd isotopes (Burkhardt et al. 2016).

The deviation from a pure *s*-process deficit pattern is also apparent during normalization to $^{146}$Nd/$^{144}$Nd when inspected closely (Figure 1(b)). Though characterized by deficits in $\mu^{142}$Nd and excesses in $\mu^{145}$Nd, $\mu^{148}$Nd, and $\mu^{150}$Nd as expected for *s*-process deficit, the $\mu^{150}$Nd anomalies in early fractions are not as high as that expected from the corresponding anomaly on $\mu^{145}$Nd or $\mu^{148}$Nd for pure *s*-process deficit. For example, a $\mu^{145}$Nd anomaly of 164 ($\pm$2) ppm as in leach fraction L3 should correspond to a $\mu^{148}$Nd anomaly of ∼285 ppm and $\mu^{150}$Nd anomaly of ∼440 ppm for pure *s*-process deficit as per stellar models (Bisterzo et al. 2011), but the measured $\mu^{148}$Nd and $\mu^{150}$Nd anomalies in L3 are 304 ($\pm$5) and 357 ($\pm$5) ppm, respectively. Boyet & Gannoun (2013) have also noted similar deviations in $\mu^{150}$Nd from a pure *s*-process pattern for the enstatite chondrite leaches they analyzed but did not recognize these as nucleosynthetic anomalies due to concerns regarding analytical artifacts, especially considering the low intensities at which they have been measured. The L3 fraction that contains ∼85% of the total Nd in Tagish Lake was measured at intensities comparable to that obtained for bulk meteorites and terrestrial standards in Saji et al. (2016, 2020). The external reproducibility on $\mu^{150}$Nd under these conditions is 6–7 ppm, suggesting that the deviation from the pure *s*-process pattern of close to 80 ppm that we see in L3 is analytically robust.

The Nd isotope anomaly pattern for the late leach fractions and residue are largely complementary to that of the early leaches (Figure 1). Again, the agreement with the *s*-process Nd component does not hold true, mainly for $\mu^{150}$Nd as was the case with early leaches. Specifically, the late fractions and residue have a less negative $\mu^{150}$Nd than expected from

**Table 2**
Nd Isotope Composition of Tagish Lake Acid Leaches and Residue Normalized to $^{146}$Nd/$^{144}$Nd

| Fraction | $\mu^{142}$Nd | $\mu^{143}$Nd | $\mu^{145}$Nd | $\mu^{148}$Nd | $\mu^{150}$Nd | Amount of Nd (ng) | $^{142}$Nd (V) | $^{147}$Sm (mV) | $^{147}$Sm/$^{144}$Nd |
|---|---|---|---|---|---|---|---|---|---|
| L1-2 | $-305.4 \pm 8.9$ | $240.9 \pm 8.7$ | $148.4 \pm 6.6$ | $296 \pm 13$ | $387 \pm 16$ | 48 | 13.1 | 0.2 | 0.22 |
| L3 | $-287.7 \pm 2.5$ | $861.7 \pm 1.7$ | $164.5 \pm 2.2$ | $304.5 \pm 4.5$ | $357.1 \pm 4.6$ | 772 | 21.1 | 0.3 | 0.21 |
| L4 | $-292.5 \pm 9.4$ | $1419.9 \pm 7.4$ | $144.1 \pm 6.2$ | $325 \pm 11$ | $491 \pm 16$ | 41 | 14.2 | 0.2 | 0.18 |
| L5 | $-247 \pm 25$ | $1733 \pm 19$ | $144 \pm 18$ | $255 \pm 29$ | $386 \pm 41$ | 8 | 3.0 | 0.2 | 0.18 |
| L6 | $-71 \pm 12$ | $6227 \pm 11$ | $97.1 \pm 9.5$ | $189 \pm 18$ | $216 \pm 22$ | 22 | 8.0 | 0.3 | 0.28 |
| L7 | $500 \pm 150$ | $8190 \pm 160$ | $-180 \pm 170$ | $-140 \pm 280$ | $1330 \pm 550$ | 1 | 0.4 | 0.1 | 0.27 |
| L8 | $677 \pm 43$ | $3569 \pm 33$ | $-474 \pm 34$ | $-922 \pm 54$ | $-964 \pm 63$ | 3 | 1.0 | 0.1 | 0.10 |
| L9 | $290 \pm 120$ | $-320 \pm 140$ | $-250 \pm 100$ | $-350 \pm 320$ | $110 \pm 350$ | 1 | 0.2 | 0.3 | 0.18 |
| L10-11-12 | $33127 \pm 53$ | $-11557 \pm 37$ | $-20560 \pm 32$ | $-38099 \pm 58$ | $-44444 \pm 60$ | 3 | 0.9 | 0.4 | 0.20 |

**Note.** The uncertainties represent $2\sigma$ internal errors for single analyses and 2SE of the mean of 10 analyses for L3.

**Table 3**
Nd Isotopic Composition of Tagish Lake Leaches and Residue Obtained by Alternate Normalization Schemes

| Fraction | $\mu^{142}$Nd[a] | $\mu^{145}$Nd[a] | $\mu^{146}$Nd[a] | $\mu^{150}$Nd[a] | $\mu^{146}$Nd[b] | $\mu^{150}$Nd[b] | N |
|---|---|---|---|---|---|---|---|
| L1-2 | $-155.1 \pm 6.8$ | $73.9 \pm 6.5$ | $-148.7 \pm 6.3$ | $-52 \pm 13$ | $-197.8 \pm 6.8$ | $-4 \pm 15$ | 1 |
| L3 | $-131.7 \pm 2.2$ | $87.6 \pm 2.7$ | $-153.2 \pm 2.3$ | $-100.2 \pm 4.3$ | $-210.9 \pm 1.9$ | $-41.8 \pm 5.4$ | 10 |
| L4 | $-122.8 \pm 9.8$ | $63.3 \pm 6.3$ | $-163.5 \pm 5.7$ | $-29 \pm 14$ | $-204.1 \pm 5.6$ | $36 \pm 15$ | 1 |
| L5 | $-121 \pm 17$ | $78 \pm 17$ | $-128 \pm 14$ | $26 \pm 30$ | $-151 \pm 15$ | $105 \pm 31$ | 1 |
| L6 | $21 \pm 11$ | $51 \pm 8$ | $-95 \pm 9$ | $-61 \pm 27$ | $-136.1 \pm 9.0$ | $-35 \pm 28$ | 1 |
| L7 | $370 \pm 62$ | $-140 \pm 220$ | $70 \pm 140$ | $1650 \pm 580$ | $144 \pm 99$ | $1200 \pm 410$ | 1 |
| L8 | $206 \pm 34$ | $-260 \pm 34$ | $465 \pm 27$ | $329 \pm 45$ | $629 \pm 32$ | $153 \pm 55$ | 1 |
| L9 | $120 \pm 160$ | $-230 \pm 120$ | $180 \pm 160$ | $620 \pm 360$ | $270 \pm 130$ | $660 \pm 630$ | 1 |
| L10-11-12 | $12875 \pm 44$ | $-10898 \pm 34$ | $19744 \pm 31$ | $12437 \pm 73$ | $27181 \pm 31$ | $5223 \pm 77$ | 1 |

**Notes.**
[a] Data normalized to $^{148}$Nd/$^{144}$Nd.
[b] Data normalized to $^{148}$Nd/$^{145}$Nd.

theoretical $s$-process Nd deficit during normalization to $^{146}$Nd/$^{144}$Nd (Figure 1(b)). When normalized to $^{148}$Nd/$^{144}$Nd, this translates to a resolvable excess in $\mu^{150}$Nd that occurs along with excesses in $\mu^{142}$Nd and $\mu^{146}$Nd for fractions L7 to L10, unlike the pure $s$-process Nd component (Figure 1(a)). Notably, leach fraction L7 that likely dissolves silicates for the first time during sequential leaching has the largest $\mu^{150}$Nd excess. Note that the $\mu^{150}$Nd excess in most late fractions and residue are retained during normalization to $^{148}$Nd/$^{145}$Nd, an isotope pair consisting of dominantly $r$-process isotopes and hence unaffected by $s$-process variability (Table 3). These deviations cannot be due to analytical artifacts such as mass-independent fractionation during Nd purification as the corresponding effects on other isotopes are not observed (Saji et al. 2016). Any effect from cosmic-ray irradiation on $^{150}$Sm, which is at most at a few $\epsilon$-level (Toth et al. 2020), does not affect our corrected $\mu^{150}$Nd data beyond analytical uncertainties. As noted earlier, an elevated $\mu^{150}$Nd compared to the pure $s$-process component is also a feature of the leaches and residue of enstatite chondrites in Boyet & Gannoun (2013). The deviations we measure in Tagish Lake leaches and residue are magnified by up to 100 times due to the fact that we analyzed individual fractions without recombination as far as it was possible. Additionally, the higher precision of the $\mu^{150}$Nd data reported here as well as the use of different normalization schemes unlike previous studies allows unambiguous detection of the systematic nature of these deviations.

Because of the uncertainties regarding the astrophysics of $r$-process nucleosynthesis (e.g., Kajino et al. 2019), the solar system $r$-process component for heavy elements is derived by subtracting the $s$-process contribution from total solar system abundances. Removal from or addition of this $r$-process component to solar composition would result in isotope anomaly patterns that are perfectly complementary to the $s$-process component, unlike what we see here. This can be further evaluated on three isotope diagrams such as those shown in Figure 2. On a $\mu^{145}$Nd versus $\mu^{148}$Nd diagram, all the leach fractions and residue lie along the mixing trend between $s$-process Nd and solar Nd within uncertainties (Figure 2(a)). This is also largely the case on a $\mu^{145}$Nd versus $\mu^{146}$Nd diagram suggesting that for these isotopes, the $r$-process component calculated as an $s$-process residual sufficiently explains the observed variations (Figure 2(c)). On the other hand, on a $\mu^{150}$Nd versus $\mu^{148}$Nd or $\mu^{150}$Nd versus $\mu^{146}$Nd diagram, the leachate best-fit line is clearly distinct from the mixing line between $s$-process Nd and solar Nd and trends toward elevated $\mu^{150}$Nd values (Figure 2(b) and (d)). Note that Boyet & Gannoun (2013) also observed a similar deviation from the $s$-mixing line for enstatite chondrite ALHA77295 on a $^{142}$Nd/$^{144}$Nd versus $^{150}$Nd/$^{144}$Nd diagram but not on $^{142}$Nd/$^{144}$Nd versus $^{145}$Nd/$^{144}$Nd or $^{142}$Nd/$^{144}$Nd versus $^{148}$Nd/$^{144}$Nd diagrams. These deviations can only be explained by the presence of a distinct component enriched in $^{150}$Nd with a $^{150}$Nd/$^{148}$Nd ratio higher than that in the solar system $s$-process component. Leach fraction L7 with highly positive $\mu^{150}$Nd at largely terrestrial $\mu^{145}$Nd, $\mu^{146}$Nd, and $\mu^{148}$Nd values is a good approximation of
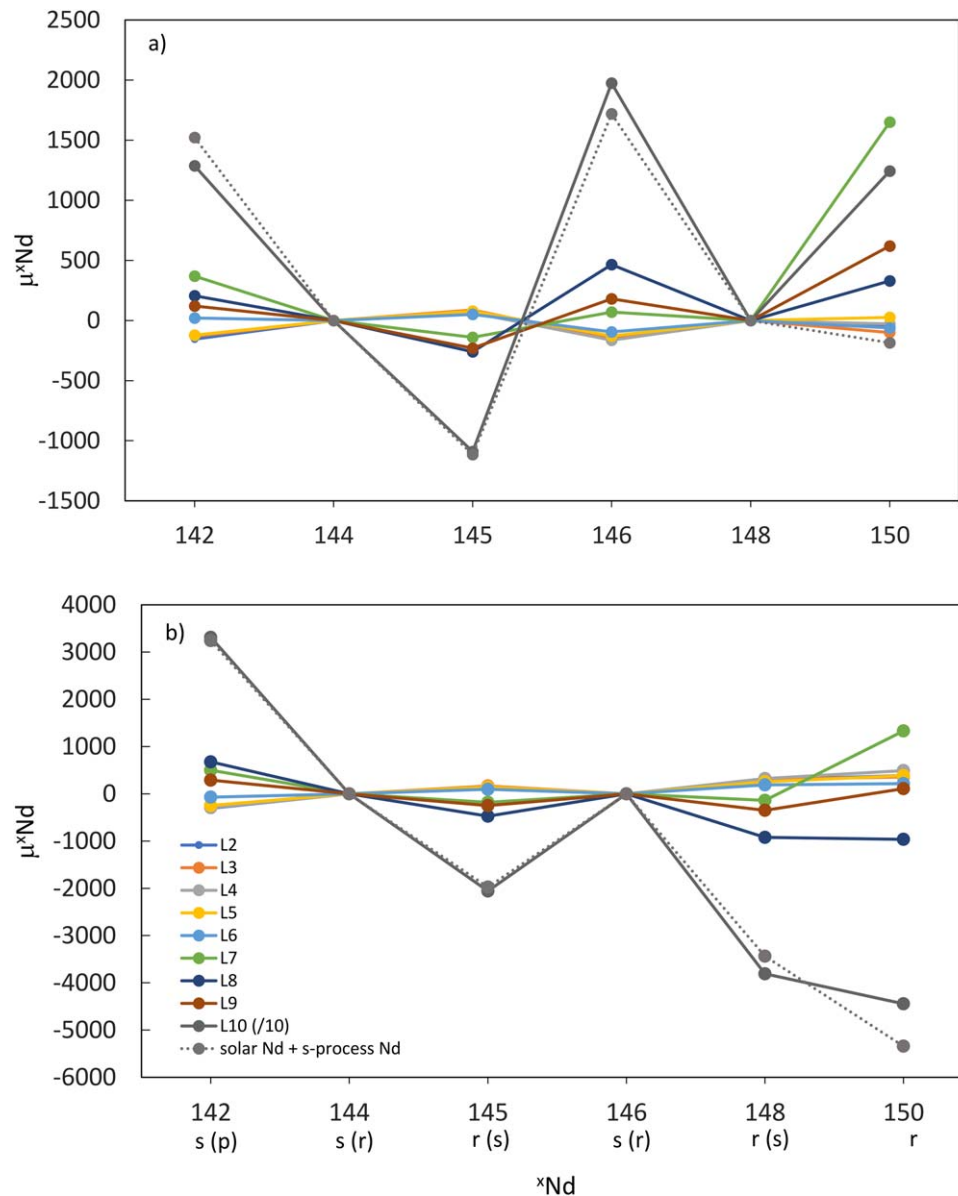
**Figure 1.** Nd isotope anomaly pattern for Tagish Lake acid leaches and residue when normalized to $^{148}Nd/^{144}Nd$ (a) and $^{146}Nd/^{144}Nd$ (b). The anomaly pattern calculated for addition of (classical) *s*-process Nd (Bisterzo et al. 2011) to solar Nd is also shown (dotted). The dominant nucleosynthetic process by which each Nd isotope is produced is shown, with the minor contribution process indicated in parentheses.

the composition of this component. We emphasize that the enrichment is most likely not just on $^{150}Nd$ and there are slight indications of deviation from the *s*-mixing line for L7 on $\mu^{145}Nd$ versus $\mu^{148}Nd$ and $\mu^{145}Nd$ versus $\mu^{146}Nd$ diagrams. However, resolving this is not possible at the analytical precision attainable on the very low Nd content of this leach fraction. The presence of an anomalous $^{150}Nd$ component in carbonaceous chondrites (CCs) was hinted at by Saji et al. (2020) from their subequal $\mu^{150}Nd$ and $\mu^{148}Nd$ values unlike that expected for *s*-process deficit. The results of our leaching experiment confirm this hypothesis and, to our knowledge, this is the first instance of identification of a non-*s*-process Nd carrier in primitive solar system materials.

## 4. Presolar Carriers of Nucleosynthetic Anomalies

Laboratory studies of presolar grains recovered from primitive meteorites have long demonstrated the presence of

a pure *s*-process signature in refractory silicon carbide (SiC) grains for many elements including Nd (Zinner et al. 1991; Richter et al. 1992; Ott 1999). The large $\mu^{142}Nd$ and $\mu^{146}Nd$ excess we measure in residue L10 that contains the most acid-resistant phases such as SiC reiterates these observations. However, one caveat with the SiC data is that the isotope composition of pure *s*-process Nd is almost always derived by assuming $^{150}Nd \simeq 0$ in line with theoretical models of *s*-process nucleosynthesis (Richter et al. 1992; Wisshak et al. 1998). Even so, the SiC data from literature show a significant deviation from *s*-process models in $\mu^{148}Nd$ versus $\mu^{150}Nd$ as well as $\mu^{146}Nd$ versus $\mu^{150}Nd$ space and agrees well with our results for Tagish Lake leaches and residue (Figure 2). This deviation has also been noted by Richter et al. (1992) and Ott (1999) in $\delta^{146}Nd$ versus $\delta^{150}Nd$ space for bulk SiC separates from Murchison where SiC compositions are clearly distinct from the *s*-process model predictions. On the other hand, there is a good agreement between meteoritic Nd and *s*-process
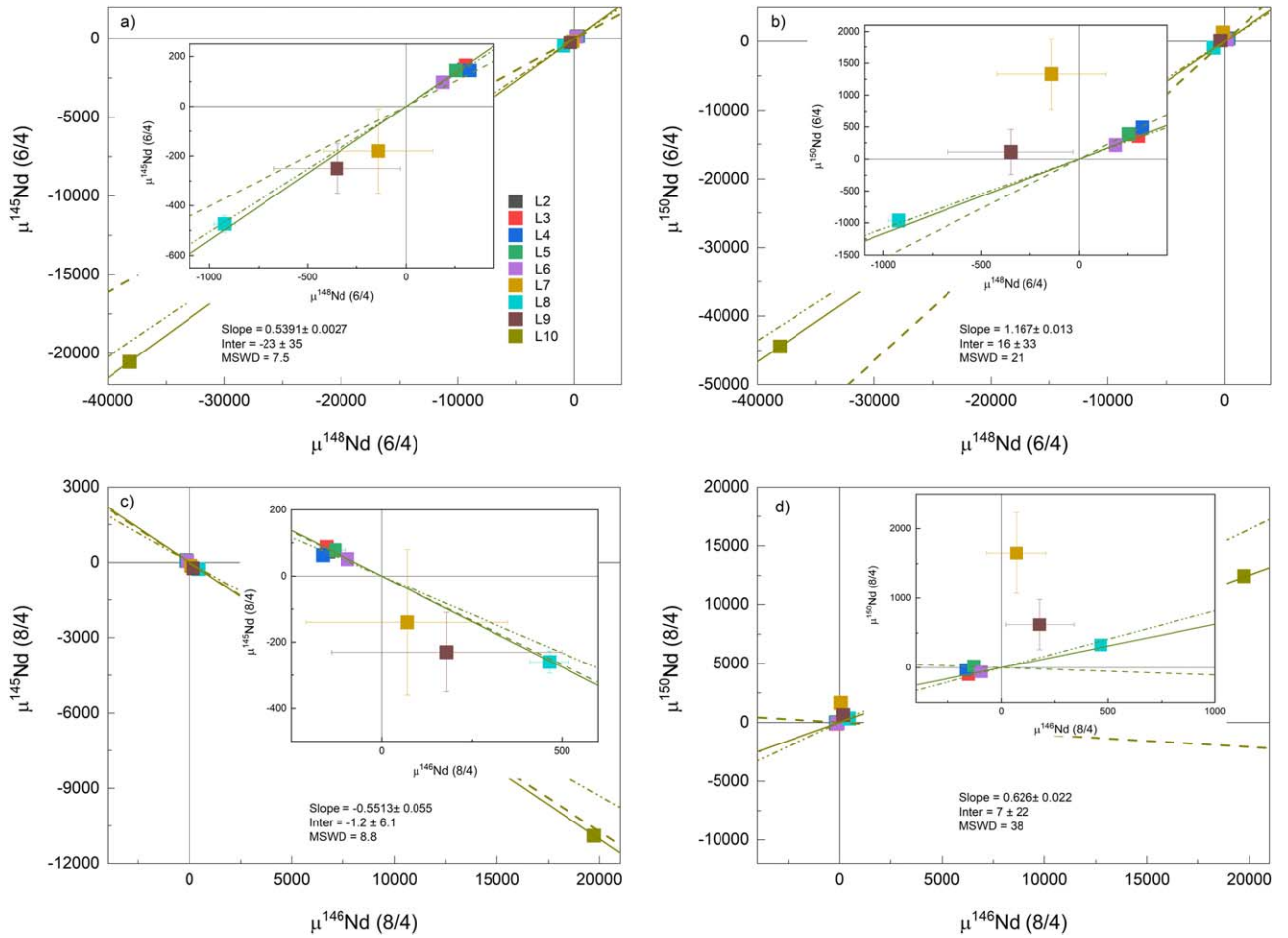
**Figure 2.** Three isotope diagrams for Tagish Lake leaches and residue with respective normalization schemes given in parentheses. Solid lines represent the leachate best-fit lines. The errors on the slopes and intercepts correspond to 95% confidence intervals calculated using *Isoplot*. The dashed line corresponds to *s*-process-mixing lines from the stellar model of Bisterzo et al. (2011) and the dotted–dashed line corresponds to SiC data from Richter et al. (1992).

models in $\mu^{145}$Nd versus $\mu^{148}$Nd or $\mu^{145}$Nd versus $\mu^{146}$Nd space for our data as well as previous leachate and presolar SiC work. What this suggests is that bulk SiC aggregates isolated from primitive meteorites are possibly mixtures of two distinct grain populations—one that carries classical *s*-process signature with origin in AGB stars and another that carries a clear $^{150}$Nd enrichment at largely solar abundances of other Nd isotopes. This is evident in the fact that Tagish Lake residue L10 plots between the pure *s*-process composition from stellar models and the anomalous $^{150}$Nd-enriched component as in leach fraction L7, defining a mixture between the two (Figure 2(b)). Our results also suggest a diversity in the carriers of both *s*-process signature and the $^{150}$Nd-enriched signature. Though the *s*-process signature is extreme in L10, the moderate *s*-excess seen in earlier leach fractions—L7 to L9 —point to the presence of labile *s*-process carriers such as silicates or oxides. Similarly, the anomalous $^{150}$Nd-enriched signature is most prominent in leach fraction L7, suggesting a labile carrier phase, though this signature is also present among refractory SiC.

Though the vast majority of presolar SiC grains studied carry an AGB *s*-process signature, SiC grains as well as other grain types that carry supernova signatures have been identified (e.g., Amari et al. 1992). These grains are possible candidates for the $^{150}$Nd-enriched component that we identify in this study. However, little data exist for their Nd isotope compositions to

make direct comparisons. Despite the lack of grain data, some qualitative inferences can be made by examining the neutron flow path in the Nd mass region. Production of $^{150}$Nd is, in principle, possible at high neutron densities that allow branching at the unstable nuclide $^{149}$Nd ($t_{1/2} = 1.73$ hr). This would require neutron densities higher than what was postulated for crossing the adjacent branching at $^{147}$Nd ($t_{1/2} = 11$ days), by activation of the $^{22}$Ne$(\alpha,n)^{25}$Mg neutron source during convective thermal pulses in AGB stars (Bisterzo et al. 2015). Most *s*-process models consider the contribution of $^{149}$Nd branching to $^{150}$Nd to be nil (Bisterzo et al. 2011, 2015). However, a recent model that include the yields from rotating massive stars unlike classical *s*-process models suggest a minor contribution from *s*-process to solar system $^{150}$Nd abundances (Prantzos et al. 2019). This can be attributed to rotational mixing that allows efficient production of $^{22}$Ne in massive stars, unlike nonrotating models in which the $^{22}$Ne neutron source is limited (Pignatari et al. 2008; Frischknecht et al. 2015). This possibly allows neutron flow to reach nuclei like $^{150}$Nd that are otherwise unreachable during the *s*-process in low- to intermediate-mass stars. Though the Maxwellian averaged cross section for $^{149}$Nd is unavailable currently, the experimentally determined neutron capture cross section for $^{149}$Nd in the MeV range is within uncertainty similar to that of $^{147}$Nd (Wang et al. 2019). Note that $^{147}$Nd has a Maxwellian averaged cross section of 544 mb (Toukan et al. 1995), permitting *s*-process production of $^{148}$Nd when $^{22}$Ne neutron source is activated in low- to

intermediate-mass AGB stars (Bisterzo et al. 2015). Collectively, this could indicate that activation of the neutron capture channel at $^{149}$Nd to produce $^{150}$Nd is feasible at sufficiently high neutron fluences when the decay barrier can be overcome.

Apart from the nonclassical $s$-process operating in rotating massive stars, another scenario where the higher neutron densities required for $^{150}$Nd production from $s$-process reaction flow are viable involves the intermediate neutron capture process or $i$-process (e.g., Hampel et al. 2016; Roederer et al. 2016). The $i$-process operates at neutron densities intermediate between the classical $s$- and $r$-processes, and occurs when rapid H-ingestion into the He-burning shell triggers a late $^{13}$C($\alpha$,n)$^{16}$O neutron source in low-mass, low-metallicity AGB or post-AGB stars (Lugaro et al. 2009; Herwig et al. 2011). Alternate sites for $i$-process nucleosynthesis include super-AGB stars that eventually explode as electron-capture supernovae or rapidly accreting white dwarfs in a binary system that explode as Type 1a supernovae (Doherty et al. 2014; Jones et al. 2015). Evidence for $i$-process nucleosynthesis exists in primitive meteorites in the form of rare presolar SiC grains with unusually low $^{134}$Ba compositions that cannot be explained by the classical $s$-process (Liu et al. 2014). This depletion in $^{134}$Ba is interpreted as bypassing of the branching point at $^{134}$Cs at neutron densities higher than that in the $s$-process. A similar scenario can be envisaged for the $^{150}$Nd excess we observe in Tagish Lake leaches and the half-life of $\sim$21 hr for $^{134}$Cs at stellar temperatures (Takahashi & Yokoi 1987) is not dramatically higher than that of $^{149}$Nd ($\sim$2 hr) implying similarly high neutron densities for crossing both branchings. A corollary here that can be tested in future studies would be that $^{149}$Sm that receives the flow from the branching at $^{149}$Nd shows a corresponding depletion. In contrast, production of $^{150}$Nd excess by classical $r$-process should be accompanied by $^{149}$Sm excesses as this is an adjacent unshielded nuclide. Although the $i$-process was first postulated long ago (Cowan & Rose 1977), many details regarding $i$-process nucleosynthesis such as abundance patterns and stellar sites remain unconstrained (e.g., Hampel et al. 2019). It is worth noting here that the progenitors of electron-capture and Type 1a supernovae, suggested to be the sources of $^{48}$Ca- and $^{54}$Cr-rich presolar carriers identified in meteorites, are plausible $i$-process sites (Wanajo et al. 2013; Schiller et al. 2015; Nittler et al. 2018). Future investigations are necessary to constrain the nucleosynthetic origin of the $^{150}$Nd-rich carrier that we identify in Tagish Lake acid leaches, and explore whether $i$-process nucleosynthesis provides an explanation for the spectrum of neutron-rich isotope anomalies seen in primitive solar system materials.

## 5. Planetary-scale Isotope Dichotomy

Several studies have identified a solar-system-wide isotope dichotomy based on the distinct enrichment of CC in neutron-rich isotopes such as $^{48}$Ca, $^{54}$Cr, $^{95,97}$Mo. etc. relative to noncarbonaceous chondrites (NCs; e.g., Trinquier et al. 2007; Nanne et al. 2019). This bifurcation of planetary materials into two isotopically distinct groups is also apparent for $^{150}$Nd, when high-precision data from our previous work is considered (Figure 3). On a $\mu^{148}$Nd versus $\mu^{150}$Nd diagram, the correlated variability for noncarbonaceous meteorites is broadly consistent with mixing of $s$-process Nd to solar Nd (Figure 3(a)). On the other hand, most carbonaceous meteorites plot off the $s$-mixing trend toward somewhat lower $\mu^{150}$Nd values. This trend is most dominant for calcium-aluminum-rich inclusions

(CAIs) and their mineral components, the oldest dated solids in the solar system (Connelly et al. 2012; Marks et al. 2014; Burkhardt et al. 2016; Bouvier & Boyet 2016). This signature can only be explained if the gaseous reservoir from which CAIs condensed is depleted in the $^{150}$Nd-enriched carrier that we identify in Tagish Lake leaches relative to solids that accreted in the terrestrial planet-forming region. Note that CAIs are in general highly enriched in the carriers of neutron-rich isotope anomalies that have defined the NC–CC dichotomy so far ($^{48}$Ca, $^{54}$Cr, $^{95,97}$Mo, etc.; Warren 2011; Budde et al. 2016; Van Kooten et al. 2016; Schiller et al. 2018; Nanne et al. 2019). The fact that CAIs are highly depleted in $^{150}$Nd relative to noncarbonaceous meteorites implies a different behavior of the carrier phase of $^{150}$Nd compared to those of other neutron-rich nuclides during planetesimal formation in the early protoplanetary disk. Notably, for all these isotopes, bulk CCs are intermediary between these two extremes.

Enrichment of carbonaceous meteorites in nuclides produced in neutron-rich stellar environments have inspired models that attribute NC–CC isotope dichotomy to a change in the composition of infalling material from the molecular cloud to the solar protoplanetary disk (e.g., Nanne et al. 2019). In these models, the outer disk where CC accreted retains the composition of the supernova dust-enriched early infall by rapid viscous spreading, whereas the inner disk where noncarbonaceous materials accreted carry the signature of supernova dust-depleted late infall. Our results are contradictory to this heterogeneous accretion scenario as the neutron-rich $^{150}$Nd-enriched carrier is depleted in CC relative to noncarbonaceous inner disk materials. Considering that $i$-process nucleosynthesis in the progenitors of Type 1a or electron-capture supernovae is a possible explanation for the $^{150}$Nd-enriched carrier, this would require supernova dust to be depleted in the carbonaceous chondrite reservoir compared to the noncarbonaceous inner disk reservoir. One way to reconcile these obvious contradictions is to attribute isotope variations to the contrasting volatility characteristics of the carriers. Alternatively, if the $^{150}$Nd-rich carrier has a stellar origin distinct from that of the carriers enriched in $^{48}$Ca, $^{54}$Cr, $^{95,97}$Mo, etc., their decoupled distribution could also be a natural consequence of solar protoplanetary disk processing dependent on carrier thermal properties. Divergent distribution of presolar dust populations as a function of their susceptibility to destruction by high-temperature or redox processes can explain the planetary-scale isotope variations including NC–CC dichotomy (Trinquier et al. 2009; Paton et al. 2013; Van Kooten et al. 2016; Schiller et al. 2018). The $^{150}$Nd-enriched carrier that we identify must be more robust to destruction by disk processes than the carriers of other neutron-rich isotope anomalies in order to explain the depletion of the former and the enrichment of the latter in the CAI-forming gas. Highly processed solids in the inner disk would have a residual enrichment of the $^{150}$Nd-enriched carrier compared to CC that accreted in the outer disk largely unprocessed (Figure 3(b)). This model is in line with the dynamics of cloud collapse and disk building that suggest the inner disk to be dominated by highly processed material from early infall and the outer disk to be dominated by relatively unprocessed material incorporated into the disk at larger centrifugal distances (Pignatale et al. 2018).
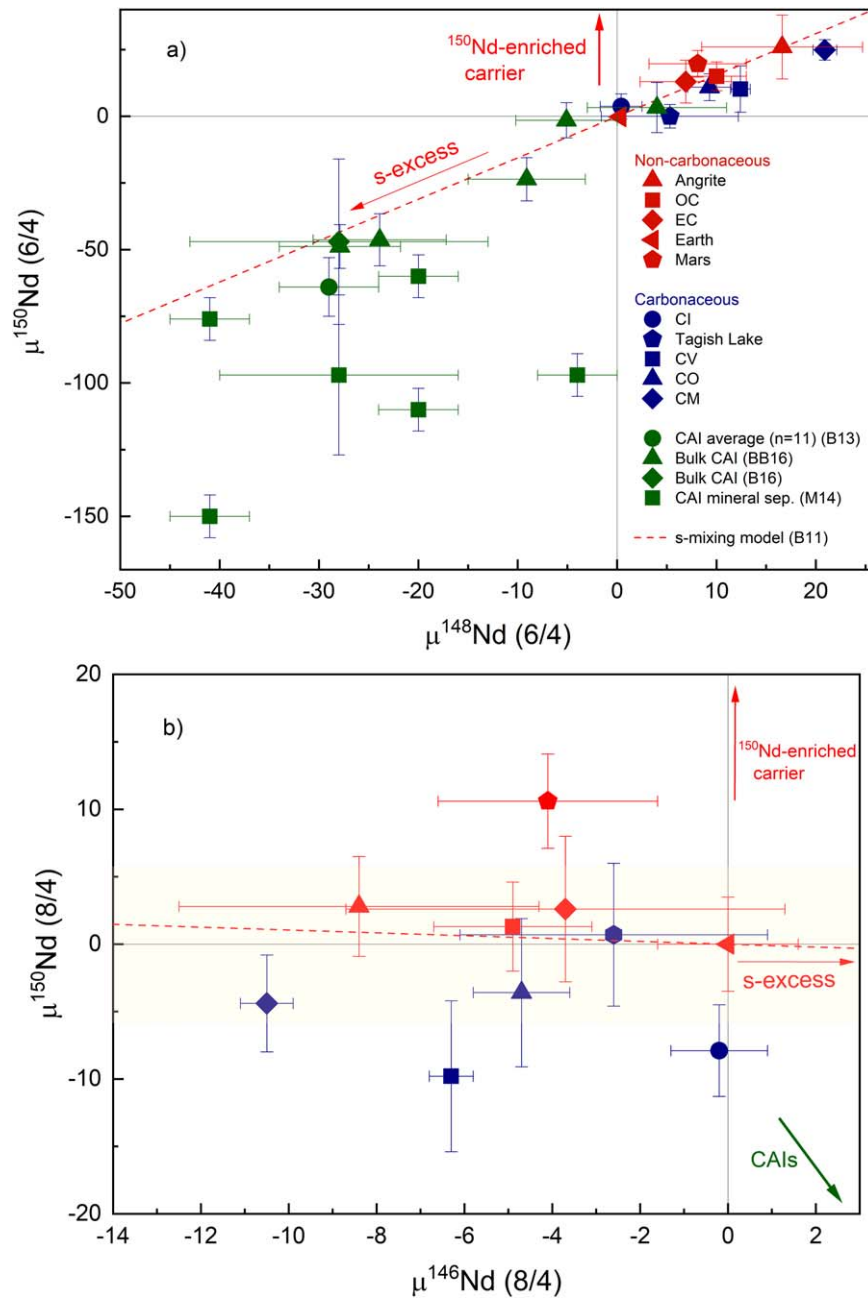
**Figure 3.** $\mu^{148}$Nd vs. $\mu^{150}$Nd diagram (a) and $\mu^{146}$Nd vs. $\mu^{150}$Nd diagram (b) for bulk meteorites and their components. The respective normalization schemes are given in parentheses. All data are from Saji et al. (2020), except for CAI data, which are from Brennecka et al. (2013), Marks et al. (2014), Burkhardt et al. (2016), and Bouvier & Boyet (2016). The s-mixing line (dashed red) is calculated using the models of Bisterzo et al. (2011). External reproducibility on $\mu^{150}$Nd from Saji et al. (2016) is shown in (b) (shaded beige).

**ORCID iDs**

Nikitha Susan Saji ● https://orcid.org/0000-0002-1843-1066
Martin Schiller ● https://orcid.org/0000-0003-4149-0627
Martin Bizzarro ● https://orcid.org/0000-0001-9966-2124

**References**

Akram, W., Schönbächler, M., Bisterzo, S., & Gallino, R. 2015, GeCoA, 165, 484
Amari, S., Hoppe, P., Zinner, E., & Lewis, R. S. 1992, ApJL, 394, L43
Arlandini, C., Käppeler, F., Wisshak, K., et al. 1999, ApJ, 525, 886
Bisterzo, S., Gallino, R., Käppeler, F., et al. 2015, MNRAS, 449, 506

Bisterzo, S., Gallino, R., Straniero, O., Cristallo, S., & Käppeler, F. 2011, MNRAS, 418, 284

Bouvier, A., & Boyet, M. 2016, Natur, 537, 399

Boyet, M., & Gannoun, A. 2013, GeCoA, 121, 652

Brennecka, G., Borg, L., & Wadhwa, M. 2013, PNAS, 110, 17241

Budde, G., Burkhardt, C., Brennecka, G. A., et al. 2016, E&PSL, 454, 293

Burkhardt, C., Borg, L. E., Brennecka, G. A., et al. 2016, Natur, 537, 394

Burkhardt, C., Kleine, T., Oberli, F., et al. 2011, E&PSL, 312, 390

Connelly, J. N., Bizzarro, M., Krot, A. N., et al. 2012, Sci, 338, 651

Cowan, J. J., & Rose, W. K. 1977, ApJ, 212, 149

Dauphas, N., Marty, B., & Reisberg, L. 2002, ApJ, 565, 640

Doherty, C. L., Gil-Pons, P., Siess, L., Lattanzio, J. C., & Lau, H. H. B. 2014, MNRAS, 446, 2599

Ek, M., Hunt, A. C., Lugaro, M., & Schönbächler, M. 2019, NatAs, 4, 273

Fischer-Gödde, M., Burkhardt, C., Kruijer, T. S., & Kleine, T. 2015, GeCoA, 168, 151

Frischknecht, U., Hirschi, R., Pignatari, M., et al. 2015, MNRAS, 456, 1803

Fukai, R., & Yokoyama, T. 2017, E&PSL, 474, 206

Hampel, M., Karakas, A. I., Stancliffe, R. J., Meyer, B. S., & Lugaro, M. 2019, ApJ, 887, 11

Hampel, M., Stancliffe, R. J., Lugaro, M., & Meyer, B. S. 2016, ApJ, 831, 171

Herwig, F., Pignatari, M., Woodward, P. R., et al. 2011, ApJ, 727, 89

Hoppe, P., & Ott, U. 1997, in AIP Conf. Proc. 402, Astrophysical Implications of the Laboratory Study of Presolar Materials, ed. T. J. Bernatowicz & E. Zinner (Melville, NY: AIP), 27

Jones, S., Ritter, C., Herwig, F., et al. 2015, MNRAS, 455, 3848

Kajino, T., Aoki, W., Balantekin, A., et al. 2019, PrPNP, 107, 109

Lichtenberg, T., Drażkowska, J., Schönbächler, M., Golabek, G. J., & Hands, T. O. 2021, Sci, 371, 365

Liu, N., Savina, M. R., Davis, A. M., et al. 2014, ApJ, 786, 66

Lugaro, M., Campbell, S. W., & de Mink, S. E. 2009, PASA, 26, 322

Marks, N., Borg, L., Hutcheon, I., Jacobsen, B., & Clayton, R. 2014, E&PSL, 405, 15

Nanne, J. A., Nimmo, F., Cuzzi, J. N., & Kleine, T. 2019, E&PSL, 511, 44

Nittler, L. R., Alexander, C. M. O., Liu, N., & Wang, J. 2018, ApJ, 856, L24

Ott, U. 1999, ScPr, 82, 49

Paton, C., Schiller, M., & Bizzarro, M. 2013, ApJL, 763, L40

Pignatale, F. C., Charnoz, S., Chaussidon, M., & Jacquet, E. 2018, ApJ, 867, L23

Pignatari, M., Gallino, R., Meynet, G., et al. 2008, ApJ, 687, L95

Prantzos, N., Abia, C., Cristallo, S., Limongi, M., & Chieffi, A. 2019, MNRAS, 491, 1832

Qin, L., Carlson, R. W., & Alexander, C. M. O. 2011, GeCoA, 75, 7806

Richter, S., Ott, U., & Begemann, F. 1992, in Lunar Planet. Sci. Conf. XXIII, 23, 1147

Roederer, I. U., Karakas, A. I., Pignatari, M., & Herwig, F. 2016, ApJ, 821, 37

Saji, N., Wielandt, D., Paton, C., & Bizzarro, M. 2016, Journal of Analytical Atomic Spectrometry, 31, 1490

Saji, N. S., Wielandt, D., Holst, J. C., & Bizzarro, M. 2020, GeCoA, 281, 135

Schiller, M., Bizzarro, M., & Fernandes, V. A. 2018, Natur, 555, 507

Schiller, M., Paton, C., & Bizzarro, M. 2015, GeCoA, 149, 88

Steele, R. C. J., Coath, C. D., Regelous, M., Russell, S., & Elliott, T. 2012, ApJ, 758, 59

Takahashi, K., & Yokoi, K. 1987, ADNDT, 36, 375

Toth, E. R., Fehr, M. A., Friebel, M., & Schönbächler, M. 2020, GeCoA, 274, 286

Toukan, K. A., Debus, K., Käppeler, F., & Reffo, G. 1995, PhRvC, 51, 1540

Trinquier, A., Birck, J.-L., & Allegre, C. 2007, ApJ, 655, 1179

Trinquier, A., Elliott, T., Ulfbeck, D., et al. 2009, Sci, 324, 374

Van Kooten, E. M. M. E., Wielandt, D., Schiller, M., et al. 2016, PNAS, 113, 2011

Wanajo, S., Janka, H.-T., & Müller, B. 2013, ApJL, 767, L26

Wang, Q., Chen, B., Zhang, Q., et al. 2019, Nucl. Sci. Tech., 30, 8

Warren, P. H. 2011, E&PSL, 311, 93

Wisshak, K., Voss, F., Käppeler, F., Kazakov, L., & Reffo, G. 1998, PhRvC, 57, 391

Zinner, E., Amari, S., & Lewis, R. S. 1991, ApJL, 382, L47